

Quantum electron liquid and its possible phase transition

Sunghun Kim

Korea Advanced Institute of Science and Technology

Joonho Bang

Sungkyunkwan University

Chan-young Lim

Korea Advanced Institute of Science and Technology

Seung Yong Lee

Sungkyunkwan University

Jounghoon Hyun

Korea Advanced Institute of Science and Technology

Gyubin Lee

Korea Advanced Institute of Science and Technology

Yeonghoon Lee

Korea Advanced Institute of Science and Technology

Jonathan Denlinger

Lawrence Berkeley National Lab <https://orcid.org/0000-0001-7645-1631>

Soonsang Huh

Seoul National University

Changyoung Kim

Seoul National University <https://orcid.org/0000-0003-0555-2341>

Seong-Gon Kim

Mississippi State University

Young Hee Lee

Institute for Basic Science <https://orcid.org/0000-0001-7403-8157>

Yeong Kwan Kim

Korea Advanced Institute of Science and Technology

Sung Wng Kim (✉ kimsungwng@skku.edu)

Sungkyunkwan University <https://orcid.org/0000-0002-4802-5421>

Article

Keywords: quantum electrons, electron-electron interaction, crystal

Posted Date: April 23rd, 2021

DOI: <https://doi.org/10.21203/rs.3.rs-445324/v1>

License:  This work is licensed under a Creative Commons Attribution 4.0 International License.

[Read Full License](#)

Version of Record: A version of this preprint was published at Nature Materials on September 29th, 2022.

See the published version at <https://doi.org/10.1038/s41563-022-01353-8>.

Quantum electron liquid and its possible phase transition

Sunghun Kim^{1,†}, Joonho Bang^{2,†}, Chan-young Lim^{1,†}, Seung Yong Lee², Jounghoon Hyun¹, Gyubin Lee¹, Yeonghoon Lee¹, Jonathan D. Denlinger³, Soonsang Huh^{4,5}, Changyoung Kim^{4,5}, Seong-Gon Kim⁶, Young Hee Lee^{2,7}, Yeongkwan Kim^{1,*}, and Sung Wng Kim^{2,7,*}

¹Department of Physics, Korea Advanced Institute of Science and Technology, Daejeon 34141, Korea.

²Department of Energy Science, Sungkyunkwan University, Suwon 16419, Korea.

³Advanced Light Source, Lawrence Berkeley National Laboratory, Berkeley, California 94720, USA.

⁴Center for Correlated Electron Systems, Institute for Basic Science, Seoul, 08826, Korea.

⁵Department of Physics and Astronomy, Seoul National University, Seoul, 08826, Korea.

⁶Department of Physics & Astronomy and Center for Computational Sciences, Mississippi State University, Mississippi States, Mississippi 39792, USA.

⁷Center for Integrated Nanostructure Physics, Institute for Basic Science, Sungkyunkwan University, Suwon 16419, Korea.

†These authors contributed equally to this work.

*E-mail: yeongkwan@kaist.ac.kr, kimsungwng@skku.edu

Abstract

Pure quantum electrons render intriguing correlated electronic phases by virtue of quantum fluctuations in addition to an exclusive electron-electron interaction. To realise such quantum electron systems, a key ingredient is dense electrons decoupled from other degrees of freedom. Here, we report the discovery of a pure quantum electron liquid, which spreads up to $\sim 3 \text{ \AA}$ in the vacuum on the surface of electride crystal. An extremely high electron density and its scant hybridization with underneath atomic orbitals evidence quantum and pure nature of electrons, exhibiting polarized liquid phase demonstrated by spin-dependent measurement. Further, upon reducing the density, the dynamics of quantum electrons drastically changes to that of non-Fermi liquid along with an anomalous band deformation, manifesting a possible transition to a hexatic liquid crystalline phase. Our findings cultivate the frontier of quantum electron systems, which serve as an ideal platform for exploring the correlated electronic phases in a pure manner.

Electron phases, ranging from gas, liquid, and to solid, are the foundation in physics, chemistry, and materials science. Understanding the genuineness of each electron phase, both from theoretical and experimental viewpoints in a complete range of densities and temperatures, is arguably the most essential knowledge, which has been a reference for diverse properties in many-body systems¹⁻³. In particular, two-dimensional (2D) electron phases have been one of the central topics as a universal phenomenon emerging in diverse systems that include 2D gas at the interface of solid materials^{4,5}, on the surface of topological insulators^{6,7}, and correlated 2D Coulomb liquid and solid on the surface of liquid helium (LHe)⁸⁻¹³. Although the theoretical and experimental approaches have been accomplished for pure 2D electron systems in the classical regime of low density, it has been challenging to experimentally realise the pure 2D electron systems in the quantum regime, which allow the access toward exotic electronic phases only expected in the quantum regime, to substantiate their theoretical predictions¹⁴⁻¹⁸ and provide a new background for their dynamics and transitions.

To realise pure 2D quantum electron systems, the prerequisite is decoupling the high-density 2D confined electrons from other degrees of freedom. Such decoupling is possible when electrons are captured on the positively charged surface of solid matter. Such quantum electrons can be found at the surface of 2D electride crystals¹⁹⁻²¹, which consist of positively charged cationic layers and counter-anionic electrons located in the interlayer space. The interstitial anionic electrons (IAEs) are localised at the interstitial space between cationic layers, not bound to the atomic orbitals of neighbouring cations. When the positively charged cationic layer is terminated at the surface of 2D electrides, the IAEs are inevitably detained on the terminated cationic layers due to the charge neutrality as the distinct surface state from IAEs. It is notable from the geometrical aspect that the theoretical maximum density of the electrons

on the surface can be as high as $\sim 9.5 \times 10^{14} \text{ cm}^{-2}$, which is expected from the concentration of IAEs in a single interlayer space of the 2D electrides with the bulk electron density of $1.4 \times 10^{22} \sim 2.9 \times 10^{22} \text{ cm}^{-3}$ (ref. 19–21). Through the experiments, the uncharted high-density pure 2D electron system with the concentration of $\sim 2.0 \times 10^{14} \text{ cm}^{-2}$ is confirmed to be realised on the surface of 2D $[\text{Gd}_2\text{C}]^{2+}\cdot 2\text{e}^-$ electride at high temperatures around 10 K, extending the phase diagram of pure 2D electrons to the quantum regime (Fig. 1a).

What is more surprising is that the pure 2D quantum electrons guarantee a scant hybridisation with the atomic orbitals of the outermost Gd elements of 2D $[\text{Gd}_2\text{C}]^{2+}\cdot 2\text{e}^-$ electride. Density functional theory (DFT) calculations clearly show two distinct electronic states of localised IAEs at the interlayer and surface electrons on the terminated cationic layer, distinguished by the electron localisation function (ELF). Figure 1b–d shows the ELFs of the 2D $[\text{Gd}_2\text{C}]^{2+}\cdot 2\text{e}^-$ electride with strongly localised IAEs and finitely delocalised surface electrons. While the IAEs have the local maxima between cationic layers, the ELF on the surface spreads up to $\sim 3 \text{ \AA}$ from the outermost Gd atoms, revealing the existence of loosely confined 2D electrons. In experiments using the 2D $[\text{Gd}_2\text{C}]^{2+}\cdot 2\text{e}^-$ electride²¹ (Extended Data Fig. 1), we verify the pure 2D quantum electrons by exposing the localised IAEs on the surface of the outermost cationic layer via in-situ cleaving at 10 K under ultra-high vacuum (UHV) better than 4×10^{-11} Torr. Angle-resolved photoemission spectroscopy (ARPES) observation clearly visualises a parabolic energy band near the Γ -point dispersing within the low binding energy region of $\sim 250 \text{ meV}$ from the Fermi energy (E_F) and V-shape band in higher energies (Fig. 2a). While the latter and other complex bands are of IAEs and cationic layers, respectively²¹, the parabolic band comes from the surface electrons above the cationic layer and has a 2D nature supported by a negligible dispersion along the k_z -axis and an isotropic

nature by a circular Fermi surface topology in the k_x - k_y plane (Extended Data Figs. 2d and 3a–c).

Most importantly, the pure nature of 2D surface electrons, i.e., free from the orbital network, is disclosed from the negligible contribution of Gd atomic orbital to the parabolic band, which is identified by DFT calculations and further confirmed by experimental observations. Figure 2b–d represents the fat band analysis that gives a clear feature for the band characters of the surface electrons and the trapped IAEs inside the bulk. The bands of the IAEs have significant contributions of Gd atomic orbitals, mostly from $5d$ and weak but finite contribution from $6s$ and $4f$ orbitals. Different from the IAE bands, there is almost no Gd orbital contribution on the parabolic band, indicating negligible overlap between surface electrons and underneath Gd orbitals, contradicting a conventional surface state in which electrons are bound around the atomic orbitals. From the resonance behaviour in photoemission intensity for each band, distinct degrees of Gd orbital contribution are identified. Band dispersions observed at 144 eV and 148 eV of photon energies (Fig. 2e,f), which correspond to off- and on-resonant condition of Gd $4d$ core level, respectively, show that the IAE band exhibits a resonance behaviour; the dramatically increased intensity at on-resonant condition (I_{IAE} , brown in Fig. 2g) caused by the finite overlap with Gd orbital. Meanwhile, the parabolic band of surface electrons gives almost intact intensity (I_{Surface} , blue in Fig. 2g), which is more apparent in the intensity ratio of $I_{\text{Surface}}/I_{\text{IAE}}$ (black in Fig. 2g), confirming a scant hybridisation between their wave functions and the outermost Gd orbitals, a pure nature of 2D surface electrons.

Having evidence that these surface electrons are successfully isolated from other degrees of freedom of the electrified solid, the next questions to be addressed are whether the pure electron system is within the desired quantum regime and which quantum phase evolves

by electron-electron interactions. Fitting the parabolic band gives an effective mass (m^*) of $\sim 2.1 m_e$ and extremely high density (n) of $\sim 2.0 \times 10^{14} \text{ cm}^{-2}$ (Fig. 3a,b), in contrast to other 2D electron gases bound to the atomic nuclei with a small m^* value in the range of $0.5\text{--}1.4 m_e$ (ref. 23–25) and to the surface electrons on the LHe with a low density of $< 10^9 \text{ cm}^{-2}$ in the classical regime^{10,11}. The extracted scattering rate of the surface electrons by measuring the peak width in the spectra reveals the liquid nature with a clear quadratic energy dependence, which corresponds to the behaviour of Fermi liquid^{26,27} (Fig. 3c). The high density over the critical boundary of the solid red line in Fig. 1a verifies that the electron liquid is in the quantum regime. Furthermore, our quantum electron liquid is spin-polarised, as verified by the spin-resolved measurements that support the spin-polarised band of the surface electrons, which is also revealed by DFT calculations (Fig. 3d). Four sets of spin-dependent spectra are obtained for the surface electrons and the trapped IAEs along out-of-plane and in-plane directions (Fig. 3f–i). It is evident that the spin polarization of the quantum electron liquid occurs in the out-of-plane direction. Meanwhile, the IAEs have a spin polarization along the in-plane direction, corresponding to the magnetic easy-axis of ferromagnetic bulk $[\text{Gd}_2\text{C}]^{2+}\cdot 2\text{e}^-$ electride, which is induced by the exchange interaction of magnetic quasi-atomic IAEs with Gd atoms of cationic layers²¹. We note that the different direction of spin polarization between the quantum electron liquid and trapped IAEs implies that the polarised nature of surface electrons is not relevant to the magnetic moment of the underlying bulk, but is likely induced by the intrinsic electron-electron interaction, as it is one of the predicted ground states of pure 2D quantum electron phases^{14–16}. Therefore, in short, unprecedented pure 2D quantum electron liquid is demonstrated, which substantiates that the polarised Fermi liquid can emerge between paramagnetic Fermi liquid and crystalline electron phases in the quantum regime^{14–16} (Fig. 1a).

Realising the pure 2D quantum electron liquid assures that the exotic phases expected in the quantum regime are ready to be explored by modifying the electron density of our polarised quantum liquid phase. The potassium (K) deposition triggers the decrease in the electron density of the quantum liquid (Extended Data Fig. 5). This can be understood with the ultralow work function of electrified system, in particular for the loosely bound surface state to the topmost atomic layer. Upon the progressive K deposition, we observed an anomalous band deformation of the quantum electrons from the initial parabolic dispersion (Fig. 4a) with an isotropic circular Fermi surface topology (Fig. 4b) to the W-shaped dispersion (Fig. 4a) with an anisotropic hexagonal topology (Fig. 4c and Extended Data Fig. 6).

We discuss the origin of the anomalous W-shaped band dispersion against the conventional band renormalisations. The deformed hexagonal topology of the quantum electrons indicates the breaking of continuous rotational symmetry. Meanwhile, when the spatial ordering of deposited K atoms occurs on the surface, the band renormalisation such as a band folding can take place, inducing the deformation of the parabolic band. However, we rule out the band folding effect on the W-shaped band dispersion from the fact that the replica bands do not appear in the higher orders of reduced Brillouin zone (BZ), which should occur if the deposited K orders and the quantum electrons strongly affected by the K ordering (Extended Data Fig. 7). The intact V-shape IAE band also supports that the ordering of deposited K atoms is unlikely.

Another possibility is that the K deposition can turn on the effect of underlying lattice, which inevitably induces the band deformation of the quantum electrons into the V-shape around zero momentum, mimicking the IAE band (Extended Data Fig. 8). However, we observed the W-shaped band dispersion around zero momentum, excluding the crystal field

effect of underlying lattice. Indeed, the absence of resonance behaviour of quantum electrons even after K deposition (Extended Data Fig. 9) strongly supports that the surface electrons are persistently in the loosely bound state and thus the negligible crystal field effect on the band deformation. Therefore, the origin of W-shape band is not attributed to the spatially modulating potentials of deposited K atoms or the terminated cationic layer. It should be noted that the observed deformation of the band dispersion, dominantly at zero momentum, occurs hardly from the change of translational symmetry.

Instead, a phase transition could be responsible for the band deformation, induced by the decreased electron density of the quantum electron liquid. Together with the reduction of band minimum energy (EBM) of surface quantum electrons, the gradual increase of m^* up to $\sim 3.9 m_e$ indicates that the electron correlation becomes stronger upon the reduction of electron density (Fig. 4a), which can trigger the phase transition^{17,18,22}. Indeed, a series of scattering rates in the sequence of K deposition shows the drastic change of energy dependence from the quadratic (#0 and #1) to linear dependence (#2, #3, and #4) (Fig. 4d,e). Note that the linear energy dependence is well-known behaviour of non-Fermi liquid²⁶⁻²⁸, strongly suggesting that the quantum electrons transit to a distinct phase, departing from Fermi liquid phase. According to the phase diagram of pure 2D electrons (Fig. 1a), a possible phase accessed by reducing the density along with the strengthened electron-electron interaction, is a hexatic phase or Wigner crystal. The remaining metallic band crossing E_F and no signature of translational symmetry change in the W-shaped band dispersion preclude the formation of Wigner crystal. It is rather reasonable to conclude that the W-shaped band dispersion is derived from a hexatic phase as the aforementioned symmetry characteristics of W-shape band are coincident with that of hexatic phase, which is a liquid crystal phase with marginally broken rotational symmetry and

preserved continuous translational symmetry^{22,29}. Our experimental observations thus suggest the emergence of hexatic phase in the quantum regime and extend the phase diagram of pure 2D electrons, which can provide a further understanding on the transition process in the quantum regime.

In summary, we discovered the unprecedented 2D quantum electron liquid on the surface of the 2D electrude crystal. The clear identification of the quantum electron liquid and its spin-polarised nature provide a step toward experimental accessibility of correlated electronic phases in the quantum regime. Indeed, the possible phase transition from the initial liquid phase to a hexatic liquid crystalline phase exhibiting non-Fermi liquid behaviour was demonstrated by the reduction of electron density and subsequent enhancement of electron correlations. Our results will stimulate the exploratory study for exotic phases in the quantum regime, such as long-lasting solid phase of pure electrons by cooling the present system and reducing the density.

METHODS

Single crystal growth. The polycrystalline $[\text{Gd}_2\text{C}]^{2+}\cdot 2\text{e}^-$ rods were synthesised by the arc melting method to prepare the feed and seed materials for the single crystal growth. The Gd metal and graphite pieces are mixed with a molar ratio of Gd:C = 2:1 in the glove box ($\text{H}_2\text{O} < 1$ ppm, $\text{O}_2 < 1$ ppm) filled with purified Ar (99.999 %) gas. The mixture was melted in an arc furnace under a high-purity Ar atmosphere. To obtain a single homogeneous phase, the melting process was repeated at least three times. After cooling, the polycrystalline $[\text{Gd}_2\text{C}]^{2+}\cdot 2\text{e}^-$ was shaped into the rods. For the single crystal growth, the floating zone melting method was performed under a high-purity Ar atmosphere to prevent oxidation. The feed and seed rods were rotated in opposite directions at the same speed of 6 rpm, with the low melt viscosity of the $[\text{Gd}_2\text{C}]^{2+}\cdot 2\text{e}^-$ electride causing a growth speed slower than 2 mm per hour. The quality of the obtained single crystal samples was checked by a combination of the X-ray diffractions (XRD) and the inductively coupled plasma (ICP) spectroscopy. The clear observation of the three-fold symmetry as a rhombohedral structure in the XRD patterns of the ϕ -scan and the negligible impurity level (all detectable impurities < 1 ppm) in the ICP results guarantee the high quality of the single crystal²¹.

ARPES measurements. ARPES measurements were performed at beamline 4.0.3 (Merlin) of the Advanced Light Source, Lawrence Berkeley National Laboratory. Sample preparations for ARPES measurements were carried out in an Ar-filled glove box to avoid contamination from water and oxygen. Single crystals of $[\text{Gd}_2\text{C}]^{2+}\cdot 2\text{e}^-$ were attached to the sample holder for ARPES and covered by ceramic top post to prepare for cleaving the sample in-situ of ARPES chamber. Both samples and top posts are fixed by silver epoxy. After curing the silver epoxy,

samples were immediately transferred to the UHV chamber for ARPES measurement. In order to obtain clean surface, samples were cleaved in-situ of UHV with pressure better than 4×10^{-11} Torr after cooling down to 10 K. Measurements were performed at the temperature of 10 K. Spectra were acquired with Scienta R8000 analyser. To obtain k_z dependent band dispersion, photon energies were set to the range between 80 eV and 110 eV with 2 eV step. Resonant ARPES measurement was performed with photon energies between 143 and 149 eV with every 1 eV step around the resonant condition of the Gd 4*d* core level (148 eV). Other data - in-plane (k_x - k_y) Fermi surface map, and band dispersions were acquired with 90 eV of photon energy. K deposition was carried out by in-situ evaporation using commercial SAES alkali metal dispensers at 10 K after cleaving the electride crystal in UHV chamber. The coverage of K was estimated from core-level spectra of K 3*p* and appearance of valence band induced by K overlayer (Extended Data Fig. 5). The total energy resolution was 25 meV or better.

Spin-resolved ARPES measurements. Spin-resolved ARPES measurements were performed at Center for Correlated Electron Systems, Institute for Basic Science. Same as ARPES measurement, sample preparations for spin-resolved ARPES measurements were carried out in an Ar-filled glove box to avoid contamination from water and oxygen, and immediately transferred to the UHV chamber for spin-resolved ARPES measurement. The clean surface was obtained by cleaving the sample in-situ of UHV with pressure better than 5.0×10^{-11} Torr after cooling down to 10 K. Measurements were performed at the temperature of 10 K. Spectra were acquired with Phoibos 225 analyser with VLEED-type spin detectors. The photon energy was 21.2 eV (He I). The total energy resolution was about 50 meV. The spin-resolved EDCs (I_{up} and I_{down}) in Fig. 3f-i are obtained from the observed spectra for different target

magnetisation (I_{+M} and I_{-M}) by following relation,

$$I_{\text{up}} = (1 + P) \cdot (I_{+M} + I_{-M})/2, I_{\text{down}} = (1 - P) \cdot (I_{+M} + I_{-M})/2$$

where P is spin polarization which can be estimated by $P = (I_{+M} - I_{-M})/(I_{+M} + I_{-M}) \cdot S_{\text{eff}}$. S_{eff} is an effective Sherman function, of which value is ~ 0.3 in the present work.

Self-energy analysis. To get the information of imaginary part of self-energy, EDCs were fitted as the ARPES intensity is nothing but the spectral function of below form,

$$A(\mathbf{k}, \omega) = -\frac{1}{\pi} \frac{\text{Im}\Sigma}{(\omega - \varepsilon_{\mathbf{k}} - \text{Re}\Sigma)^2 + \text{Im}\Sigma^2}$$

where $\text{Re}\Sigma$ is the real part of the self-energy, and $\varepsilon_{\mathbf{k}}$ is the bare band dispersion. The obtained half-width at half maximum of the Lorentzian curve is the imaginary part of self-energy ($\text{Im}\Sigma$). Prior to fitting, EDCs were divided by Fermi-Dirac distribution to avoid diminishing intensity near the Fermi level. The fitting curve involves two Lorentzian curves, lower and higher binding energies for surface electron and IAE bands, respectively. The fitted curve was convoluted with a Gaussian to encounter the experimental resolution. The resulting fit curves, multiplied by Fermi-Dirac distribution, closely reproduce the original spectra (Extended Data Fig. 4), reflected in small fitting error of $\text{Im}\Sigma$ in Figs. 3c and 4d.

Autocorrelation analysis. Autocorrelation of ARPES intensity $I_{\text{AC}}(\mathbf{q}, \omega)$ (Extended Data Fig. 6e), was calculated by substituting the symmetrised and filtered CECs into below formula^{30,31},

$$I_{\text{AC}}(\mathbf{q}, \omega) = \int I(\mathbf{k}, \omega) I(\mathbf{k} + \mathbf{q}, \omega) d\mathbf{k}$$

where $I(\mathbf{k}, \omega)$ is ARPES intensity at momentum \mathbf{k} and binding energy ω extracted by given CEC, and \mathbf{q} is momentum transfer. The three-fold symmetrisation was applied to avoid the momentum dependent modulation of intensity due to the matrix element effect. It was ensured that the symmetrisation does not deform the original shape of CECs from the surface band (Extended Data Fig. 6c,d). The signal from the outer bands was filtered out to include only the signal from the surface electron band in the analysis (Extended Data Fig. 6d).

DFT calculations. DFT calculations were performed using the generalised gradient approximation (GGA) with the Perdew-Burke-Ernzerhof (PBE) functional and the projector augmented plane-wave method implemented in the Vienna *ab initio* simulation program (VASP) code³²⁻³⁴. The $4f$, $5s$, $5p$, $5d$ and $6s$ electrons of Gd and the $2s$ and $2p$ electrons of C were used as valence electrons. The plane-wave-basis cut-off energy was set to 600 eV. The slab supercell of $a \times b \times 3c$ (27 atoms) with a vacuum layer of 20 Å along the c -axis was used for the surface calculation. Structural relaxations of the bulk and slab structures were performed using $8 \times 8 \times 2$ and $8 \times 8 \times 1$ k -point meshes until the Hellmann-Feynman forces were less than 10^{-5} and 10^{-3} eV \cdot Å⁻¹, respectively. The lattice constants of the relaxed bulk structure are well-matched with those obtained by the XRD measurement (mismatch of the lattice parameters is less than 1 %, Extended Data Fig. 1d). For the relaxation of the slab supercell, the three layers at both ends of the slab were relaxed while keeping the central three layers frozen (Extended Data Fig. 2a). The crystal structures and electron localisation functions were visualised with the VESTA code³⁵. The Fermi surface was visualised with the XCrySDen code³⁶. The virtual crystal approximation method was adopted with a Wigner-Seitz radius of 1.25 Å to consider the contribution of the surface electrons on the electronic band structure.

Data Availability

The data that support the plots in this paper and other findings of this study are available from the corresponding author upon reasonable request.

References

1. Phillips, P., Wan, Y., Martin, I., Knysh, S. & Dalidovich, D. Superconductivity in a two-dimensional electron gas. *Nature* **395**, 253–257 (1998).
2. Mannhart, J. & Schlom, D. G. Oxide interfaces—an opportunity for electronics. *Science* **327**, 1607–1611 (2010).
3. Hwang, H. Y. *et al.* Emergent phenomena at oxide interfaces. *Nat. Mater.* **11**, 103–113 (2012).
4. Tsui, D. C., Stormer, H. L. & Gossard, A. C. Two-dimensional magnetotransport in the extreme quantum limit. *Phys. Rev. Lett.* **48**, 1559–1562 (1982).
5. Ohtomo, A. & Hwang, H. Y. A high-mobility electron gas at the LaAlO₃/SrTiO₃ heterointerface. *Nature* **427**, 423–426 (2004).
6. Bianchi, M. *et al.* Coexistence of the topological state and a two-dimensional electron gas on the surface of Bi₂Se₃. *Nat. Commun.* **1**, 128 (2010).
7. Bahramy M. S. *et al.* Emergent quantum confinement at topological insulator surfaces. *Nat. Commun.* **3**, 1159 (2012).
8. Sommer, W. T. & Tanner, D. J. Mobility of electrons on the surface of liquid ⁴He. *Phys. Rev. Lett.* **27**, 1345–1349 (1971).
9. Grimes, C. C., Brown, T. R., Burns, M. L. & Zipfel, C. L. Spectroscopy of electrons in image-potential-induced surface states outside liquid helium. *Phys. Rev. B* **13**, 140–147 (1976).
10. Grimes, C. C. Electrons in surface states on liquid helium. *Surf. Sci.* **73**, 379–395 (1978).
11. Grimes, C. C. & Adams, G. Evidence for a liquid-to-crystal phase transition in a classical two-dimensional sheet of electrons. *Phys. Rev. Lett.* **42**, 795–798 (1979).
12. Andrei, E. Y. *Two-dimensional electron systems on helium and other cryogenic substrates.* (Kluwer Academic Publishers, 1997).
13. Monarkha, Y. & Kono, K. *Two-dimensional coulomb liquids and solids.* (Springer, 2004).
14. Ceperley, D. Ground state of the fermion one-component plasma: A Monte Carlo study in two and three dimensions. *Phys. Rev. B* **18**, 3126–3138 (1978).
15. Varsano, D., Moroni, S., & Senatore, G. Spin-polarization transition in the two-dimensional electron gas. *Europhys. Lett.* **53**, 348–353 (2001).
16. Attaccalite, C., Moroni, S., Gori-Giorgi, P. & Bachelet, G. B. Correlation energy and spin polarization in the 2D electron gas. *Phys. Rev. Lett.* **88**, 256601 (2002).
17. Spivak, B. & Kivelson, S. A. Phases intermediate between a two-dimensional electron liquid and Wigner crystal. *Phys. Rev. B* **70**, 155114 (2004).
18. Waintal, X. On the quantum melting of the two-dimensional Wigner crystal. *Phys. Rev. B* **73**,

- 075417 (2006).
19. Lee, K., Kim, S. W., Toda, Y., Matsuishi, S. & Hosono, H. Dicalcium nitride as a two-dimensional electride with an anionic electron layer. *Nature* **494**, 336–340 (2013).
 20. Park, J. *et al.* Strong localization of anionic electrons at interlayer for electrical and magnetic anisotropy in two-dimensional Y_2C electride. *J. Am. Chem. Soc.* **139**, 615–618 (2017).
 21. Lee, S. Y. *et al.* Ferromagnetic quasi-atomic electrons in two-dimensional electride. *Nat. Commun.* **11**, 1526 (2020).
 22. Clark, B. K., Casula, M. & Ceperley, D. M. Hexatic and mesoscopic phases in a 2D quantum Coulomb system. *Phys. Rev. Lett.* **103**, 055701 (2009).
 23. Santander-Syro, A. F. *et al.* Two-dimensional electron gas with universal subbands at the surface of $SrTiO_3$. *Nature* **469**, 189–193 (2011).
 24. Meevasana, W. *et al.* Creation and control of a two-dimensional electron liquid at the bare $SrTiO_3$ surface. *Nat. Mater.* **10**, 114–118 (2011).
 25. Wang, Z. *et al.* Tailoring the nature and strength of electron–phonon interactions in the $SrTiO_3(001)$ 2D electron liquid. *Nat. Mater.* **15**, 835–839 (2016).
 26. Damascelli, A., Hussain, Z. & Shen, Z. -X. Angle-resolved photoemission studies of the cuprate superconductors. *Rev. Mod. Phys.* **75**, 473–541 (2003).
 27. Kaminski, A. & Fretwell, H. M. On the extraction of the self-energy from angle-resolved photoemission spectroscopy. *New. J. Phys.* **7**, 98 (2005).
 28. Varma, C. M., Littlewood, P. B., Schmitt-Rink, S., Abrahams, E. & Ruckenstein, A. E. Phenomenology of the normal state of Cu-O high-temperature superconductors. *Phys. Rev. Lett.* **63**, 1996–1999 (1989).
 29. Halperin, B. I. & Nelson, D. R. Theory of two-dimensional melting. *Phys. Rev. Lett.* **41**, 121–124 (1978).
 30. Borisenko, S. V. *et al.* Pseudogap and charge density waves in two dimensions. *Phys. Rev. Lett.* **100**, 196402 (2008).
 31. Hashimoto, M. *et al.* Reaffirming the $d_{x^2-y^2}$ superconducting gap using the autocorrelation angle-resolved photoemission spectroscopy of $Bi_{1.5}Pb_{0.55}Sr_{1.6}La_{0.4}CuO_{6+\delta}$. *Phys. Rev. Lett.* **106**, 167003 (2011).
 32. Kresse, G. & Furthmüller, J. Efficient iterative schemes for *ab initio* total-energy calculations using a plane-wave basis set. *Phys. Rev. B* **54**, 11169–11186 (1996).
 33. Blöchl, P. E. Projector augmented-wave method. *Phys. Rev. B* **50**, 17953–17979 (1994).
 34. Perdew, J. P., Burke, K. & Ernzerhof, M. Generalized gradient approximation made simple. *Phys. Rev. Lett.* **77**, 3865–3868 (1996).

35. Momma, K. & Izumi, F. *VESTA 3* for three-dimensional visualization of crystal, volumetric and morphology data. *J. Appl. Crystallogr.* **44**, 1272–1276 (2011).
36. Kokalj, A. XCrySDen—a new program for displaying crystalline structures and electron densities. *J. Mol. Graph. Model.* **17**, 176–179 (1999).

Acknowledgments

This work was supported by Institute for Basic Science (IBS-R011-D1) and National Research Foundation of Korea (NRF) grant funded by the Korean government (Ministry of Science, ICT & Future Planning) (No.2015M3D1A1070639, No.2019R1A6A3A01091336, No.2020R1A4A2002828). The Advanced Light Source is supported by the Office of Basic Energy Sciences of the US DOE under contract No.DE-AC02-05CH11231. Part of this study has been performed by using facilities at IBS Center for Correlated Electron Systems, Seoul National University, Korea.

Author Contributions

S.W.K. and Y.K.K. conceived the project. S.Y.L, J.B. and S.W.K. synthesised and characterised single crystals. S.K., C.-Y.L., J.H., G.L., Y.L., J.D.D. and Y.K.K. performed ARPES measurements. S.K., J.B., S.H., C.K., and Y.K.K. carried out spin-resolved ARPES experiments. S.K., J.B., C.-Y.L, S.-G.K., Y.K.K., and S.W.K. analysed ARPES data. J.B., S.-G.K., Y.H.L., Y.K.K. and S.W.K. delivered DFT calculations. All authors discussed the results. S.K., J.B., Y.K.K. and S.W.K. prepared a manuscript with contributions from all authors.

Competing interests

The authors declare no competing interests.

Additional Information

Supplementary information is available for this paper at <https://doi.org/xxxxx>.

Correspondence and requests for materials should be addressed to Y.K.K. and S.W.K.

Peer review information *Nature Materials* thanks XXXX and the other, anonymous, reviewer(s) for their contribution to the peer review of this work.

Reprints and permission information is available at <http://www.nature.com/reprints>.

Publisher's note: Springer Nature remains neutral with regard to jurisdictional claims in published maps and institutional affiliations.

Rights and permissions

Reprints and Permissions

Figures and Figure Legends

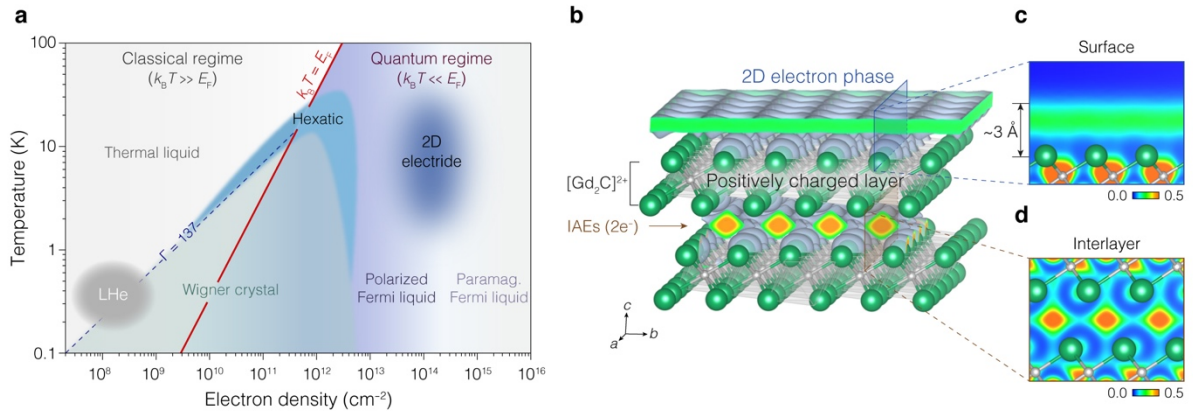


Figure 1 | Evolution of pure 2D quantum electrons. **a**, Phase diagram of pure 2D electron system in terms of electron density and temperature. The solid red line ($k_B T = E_F$) divides the quantum (right) from classical (left) regimes. Colours represent the electron phases; thermal liquid, liquid crystalline hexatic and Wigner crystal in the classical regime, and paramagnetic Fermi liquid, polarised Fermi liquid, hexatic and Wigner crystal in quantum regime. The phase boundaries are estimated from refs. 11, 14–16, 22. The electron phases on the LHe (grey area) are marked from ref. 11. Dashed blue line is the experimental estimation of Coulomb coupling parameter, $\Gamma = 137$ for the Wigner crystallisation in classical regime¹¹. The present pure 2D quantum electrons on the 2D $[\text{Gd}_2\text{C}]^{2+} \cdot 2\text{e}^-$ electride reside in the area of Fermi liquid (dark blue area). Detailed physical quantities of 2D electrons on LHe and 2D $[\text{Gd}_2\text{C}]^{2+} \cdot 2\text{e}^-$ electride are compared in Extended Data Table 1. **b–d**, Visualisation of ELFs for the electrons on the surface and at the intralayer of 2D $[\text{Gd}_2\text{C}]^{2+} \cdot 2\text{e}^-$ electride. Cross-sectional plots of the ELFs for the electrons on the surface (**c**) and IAEs at the interlayer (**d**) taken from the blue and brown windows marked in **b**, respectively.

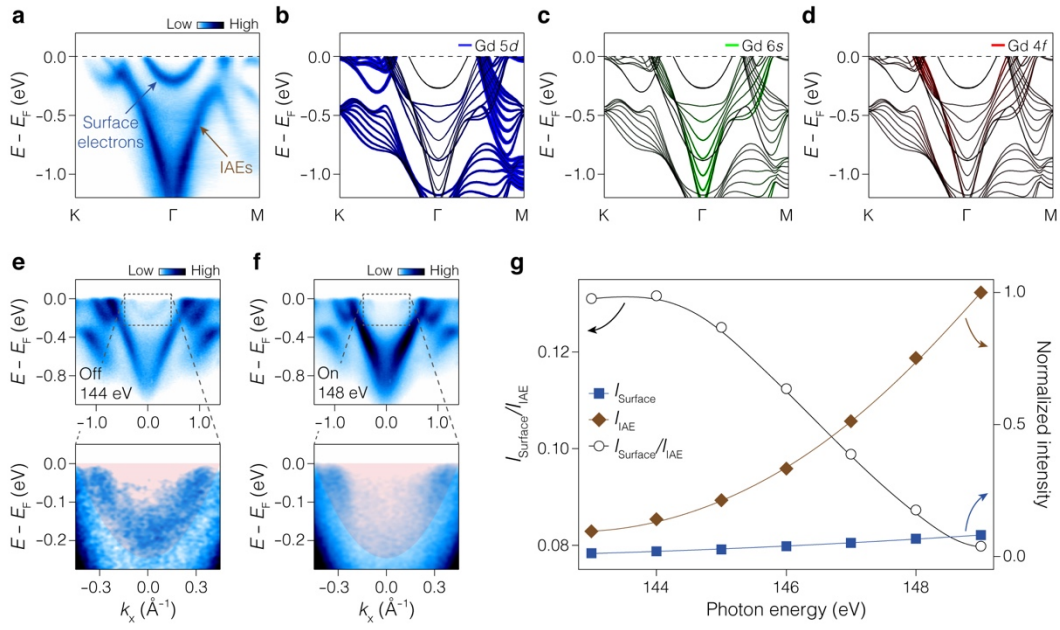


Figure 2 | Floating quantum electrons on 2D electride. **a**, Band dispersion of the 2D $[\text{Gd}_2\text{C}]^{2+}\cdot 2e^-$ observed by ARPES. The blue and brown arrows indicate the parabolic and V-shaped band dispersion from the surface electrons on the terminated $[\text{Gd}_2\text{C}]^{2+}$ layer and IAEs trapped between $[\text{Gd}_2\text{C}]^{2+}$ layers in the bulk, respectively. **b–d**, Calculated band dispersions with fat band analysis using the nine-slab model (Extended Data Fig. 2a), exhibiting the contribution of Gd 5d (**b**), 6s (**c**), and 4f (**d**) orbitals. Band thickness with different colours represents the contribution of each orbital; the thicker line has more contribution from the corresponding orbitals. The fat band width in **c** and **d** has been magnified by 2 and 3.5 times, respectively, compared with that in **b**. Almost no colour from each orbital is represented in the parabolic band. **e,f**, Band dispersions taken at off- (144 eV, **e**) and on-resonant (148 eV, **f**) condition of Gd 4d core level. Lower panels are magnified images of the boxed area in the upper panels. **g**, Normalised intensity (right) of the surface 2D electrons (I_{Surface} , blue) and IAEs (I_{IAE} , brown), and their ratio (left, black) as a function of photon energy (Extended Data Fig. 3d,e). I_{Surface} and I_{IAE} are obtained by integrating the intensity of the shaded red area in lower panels and the exclusive area of red shade in upper panels of **e** and **f**, respectively.

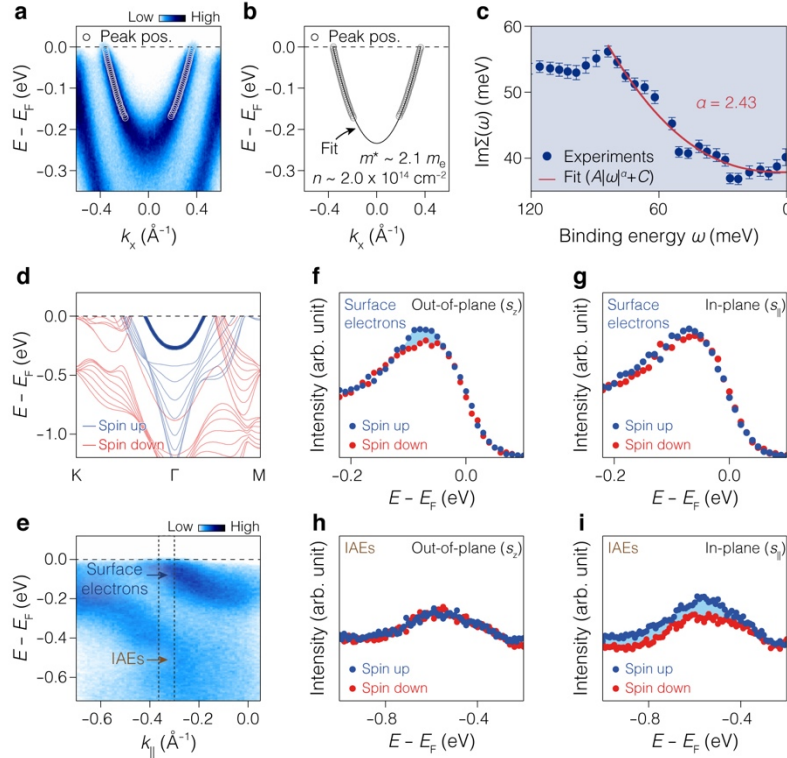


Figure 3 | Spin-polarized nature of quantum electron liquid. **a,b**, Enlarged band dispersion of surface electrons (**a**). The m^* and n of surface electrons are estimated to be $\sim 2.1 m_e$ and $\sim 2.0 \times 10^{14} \text{ cm}^{-2}$ from the quadratic fitting (black curve in **b**) of peak positions (white circles) obtained from momentum distribution curves (MDCs) in **a**. **c**, Imaginary part of self-energy, $\text{Im}\Sigma$ (filled blue circles), obtained by fitting the energy distribution curve (EDC) width (Extended Data Fig. 4), as a function of binding energy (ω). The solid red curve represents the fit with a power-law ($\text{Im}\Sigma(\omega) = A|\omega|^\alpha + C$). **d**, Calculated spin-polarised band structure with fat band for the surface electrons. Blue and red colours reflect the spin up and spin down components, respectively. A thick blue band for the surface electrons clearly indicates that the quantum electrons are spin-polarised. For the V-shape bands of the IAEs, spin-polarised state is also shown in the blue colour. **e**, Measured band dispersion for the spin-resolved ARPES. **f-i**, Spin-resolved EDCs of surface electrons (**f,g**) and IAEs (**h,i**), respectively. Spin up and spin down components are represented by blue and red dots, respectively. EDCs are obtained by integrating intensity within the dashed vertical lines in **e**.

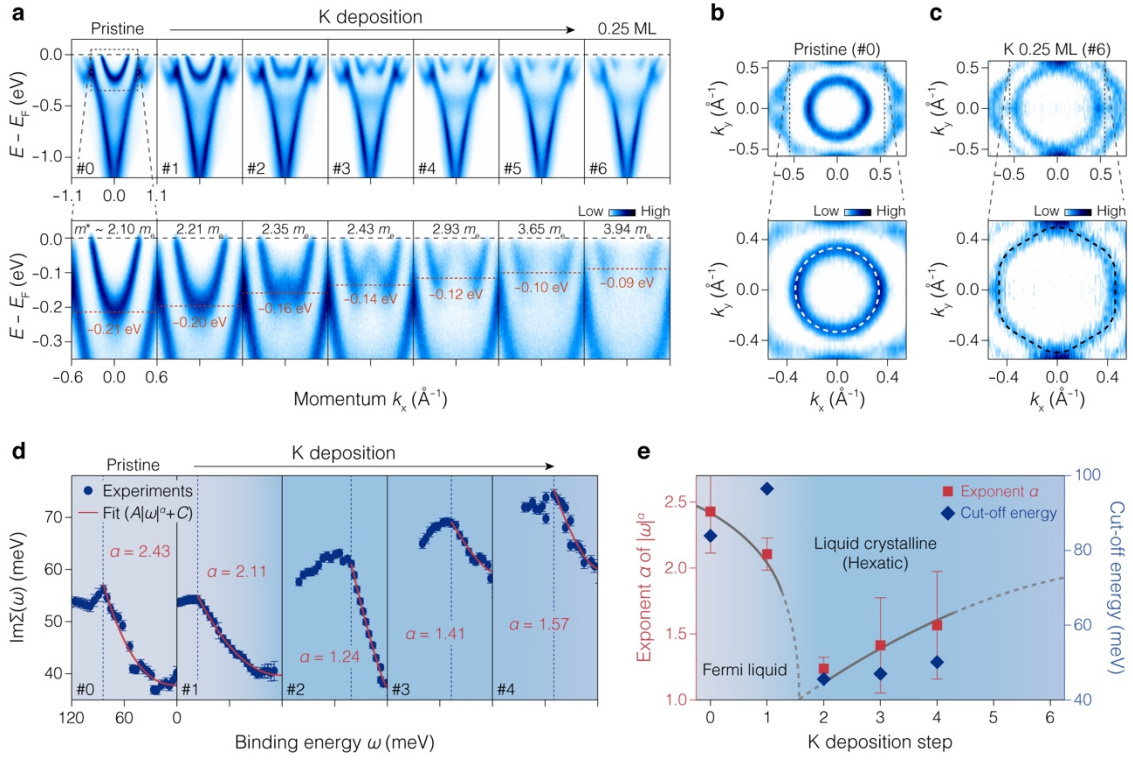
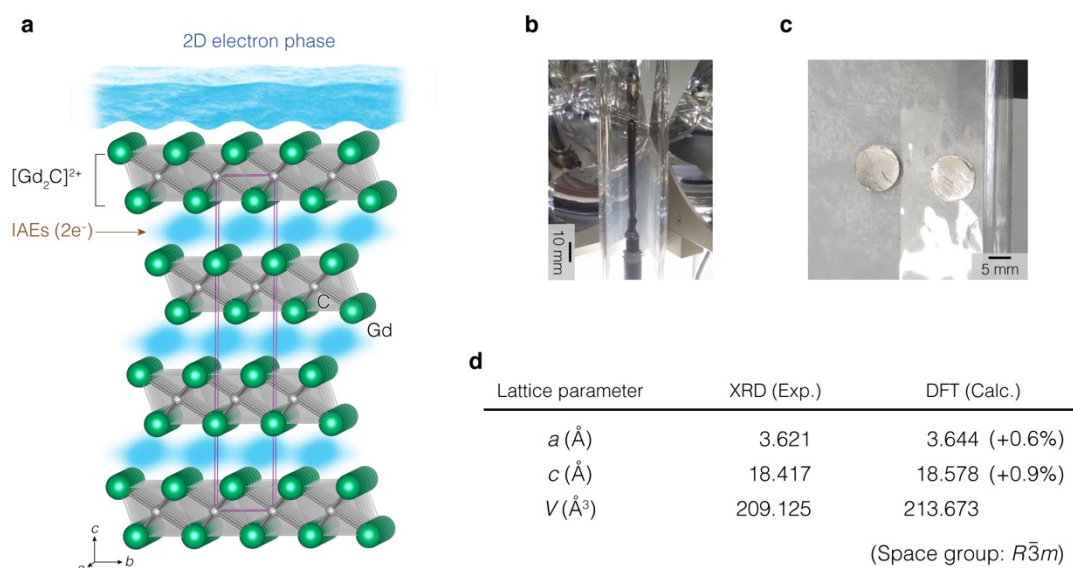
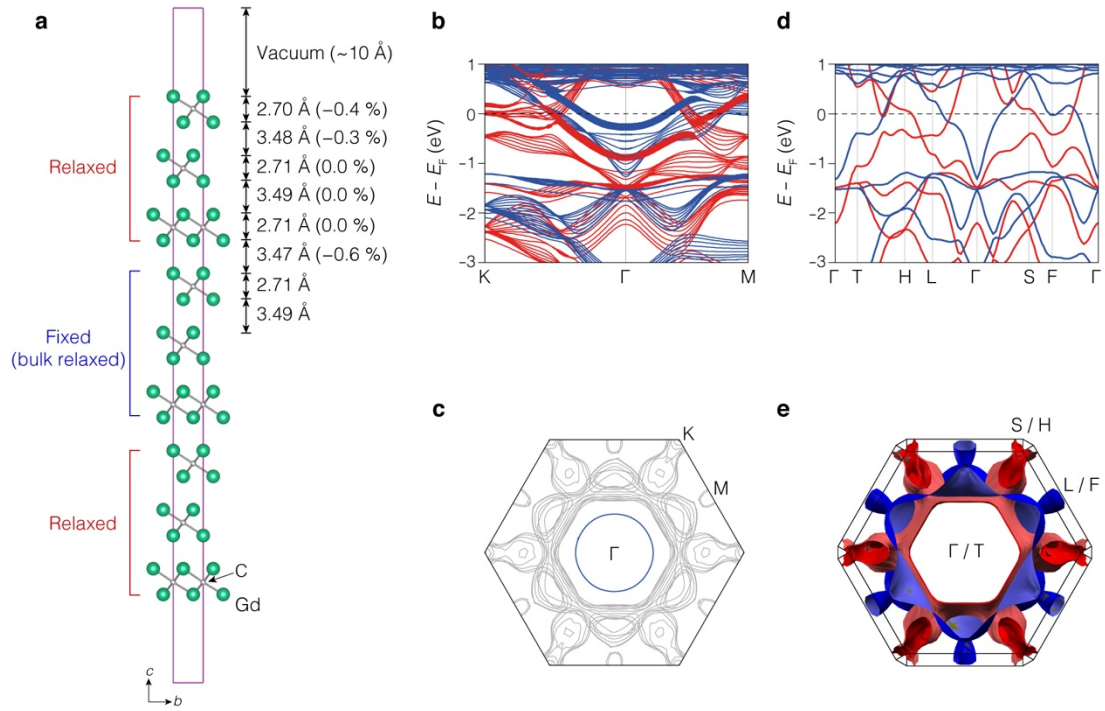


Figure 4 | Phase transition of quantum electrons. **a**, Stepwise evolution of the electronic structure upon K deposition, from the 0 ML (pristine, leftmost) up to 0.25 ML coverage (rightmost). Details of K coverage estimation are described in Extended Data Fig. 5. Lower panels show magnified images (dashed box in the leftmost upper panel) for the band of quantum electrons in each step. Dashed red lines in lower panels represent E_{BM} . **b,c**, Fermi surface in $k_x - k_y$ plane of the as-cleaved (#0, **b**) and 0.25 ML K-deposited (#6, **c**) samples. Lower panels exhibit magnified images of dashed boxes in upper panels. Dashed white circle and dashed black hexagon represent a guide for the eye of Fermi surface topology. **d**, $\text{Im}\Sigma$ for the band of quantum electrons upon K deposition step, extracted by the line shape analysis of EDCs (Extended Data Fig. 4). Solid red curves in each panel are fitted curves of $\text{Im}\Sigma(\omega)$ with a power-law. Dashed blue vertical lines indicate the cut-off energy of $\text{Im}\Sigma$. **e**, Extracted quantities of exponent α in the $\text{Im}\Sigma(\omega) = A|\omega|^\alpha + C$ and the cut-off energy as a function of the K deposition. Both exponent α (red squares) and the cut-off energy (blue diamonds) show a similar trend, having minima at a specific deposition step (#2) and then increasing toward the initial values upon K coverage. The grey curve is a guide for the eye.

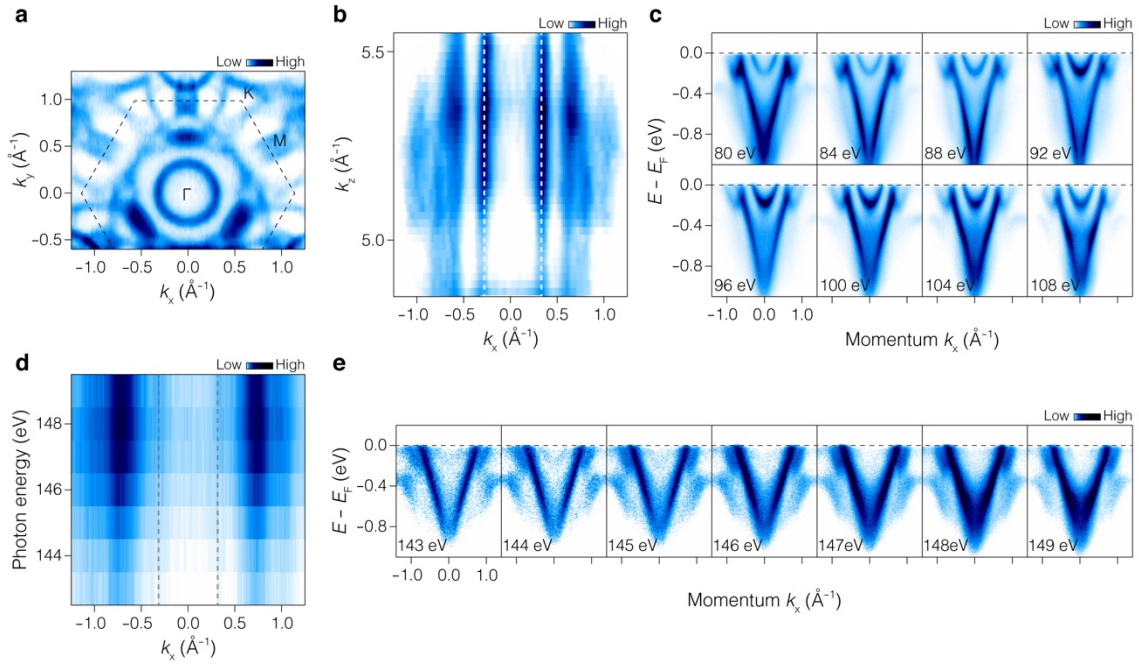
Extended data figures and tables



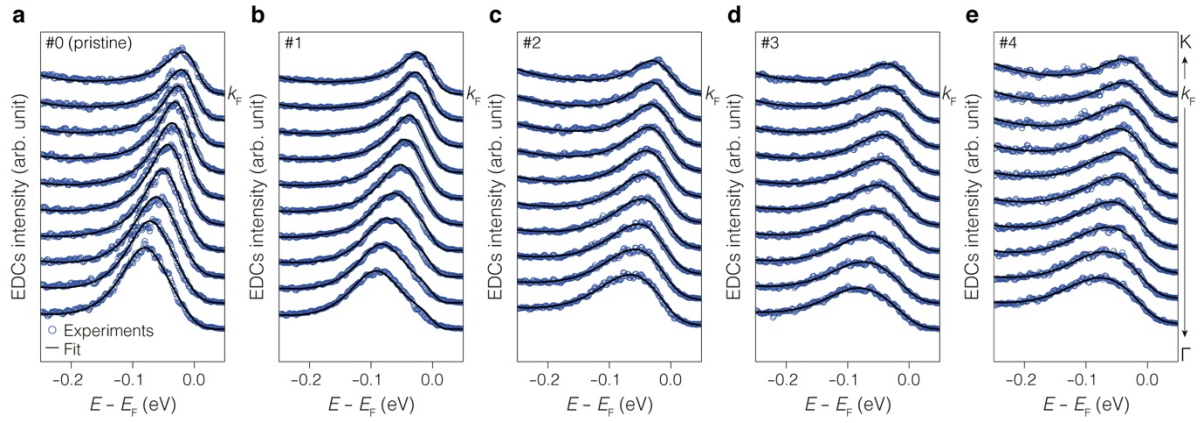
Extended Data Figure 1 | Crystal structure of the 2D $[\text{Gd}_2\text{C}]^{2+}\cdot 2\text{e}^-$ electride. **a**, Anti- CdCl_2 -type layered structure of $[\text{Gd}_2\text{C}]^{2+}\cdot 2\text{e}^-$ with a space group of $R\bar{3}m$. The cationic slab $[\text{Gd}_2\text{C}]^{2+}$ is composed of an edge-sharing octahedra structure and is separated by the interlayer space. IAEs (brown arrow) are confined between the positively charged $[\text{Gd}_2\text{C}]^{2+}$ layers. The 2D electrons distinct from IAEs are floated on the topmost $[\text{Gd}_2\text{C}]^{2+}$ layer. The purple lines indicate the unit cell. **b,c**, Photographs of single crystal $[\text{Gd}_2\text{C}]^{2+}\cdot 2\text{e}^-$ rod with 50 mm length grown by floating zone melting method (**b**) and as-cleaved crystal by 3M Scotch tape (**c**). **d**, Lattice parameters obtained by the XRD measurements²¹ and the DFT calculations.



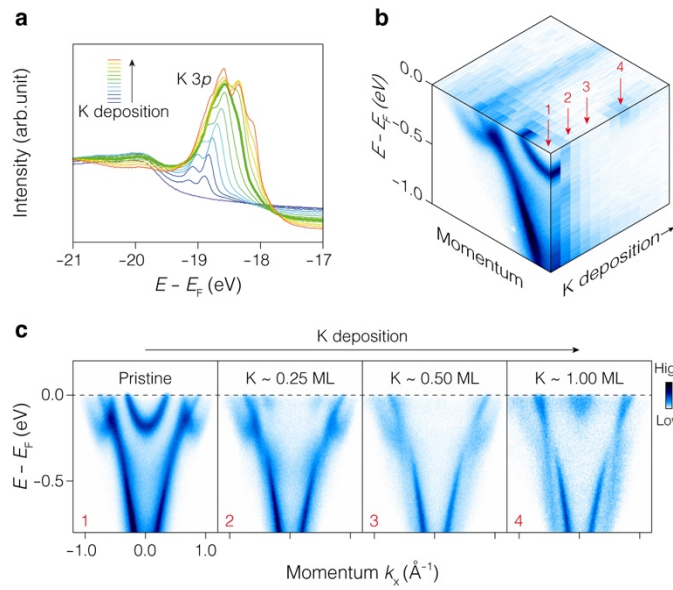
Extended Data Figure 2 | The detailed electronic structure of $[\text{Gd}_2\text{C}]^{2+}\cdot 2e^-$ obtained by DFT calculations. **a**, Relaxed crystal structure of the nine-slab model for the slab calculations. $a \times b \times 3c$ supercell with a vacuum of 20 \AA along the c -axis was used. For the relaxation of the nine-slab model, the optimised bulk structure was used for the central three-layer, while the three layers at both ends of the slab were relaxed. **b,c**, Calculated band structure and the Fermi surface of $[\text{Gd}_2\text{C}]^{2+}\cdot 2e^-$ using the nine-slab model, respectively. Blue and red colours indicate spin up and spin down components, respectively. Band thickness represents the contribution of the surface electrons. The thicker line has a contribution mainly from the surface character. **d,e**, Band structure and the Fermi surface (top view along k_z direction) of $[\text{Gd}_2\text{C}]^{2+}\cdot 2e^-$ obtained by bulk calculation, respectively. In contrast to the result from the nine-slab model, the bulk calculation does not reproduce the parabolic band dispersion with cylindrical 2D Fermi surface observed by ARPES (Fig. 2a and Extended Data Fig. 3a–c).



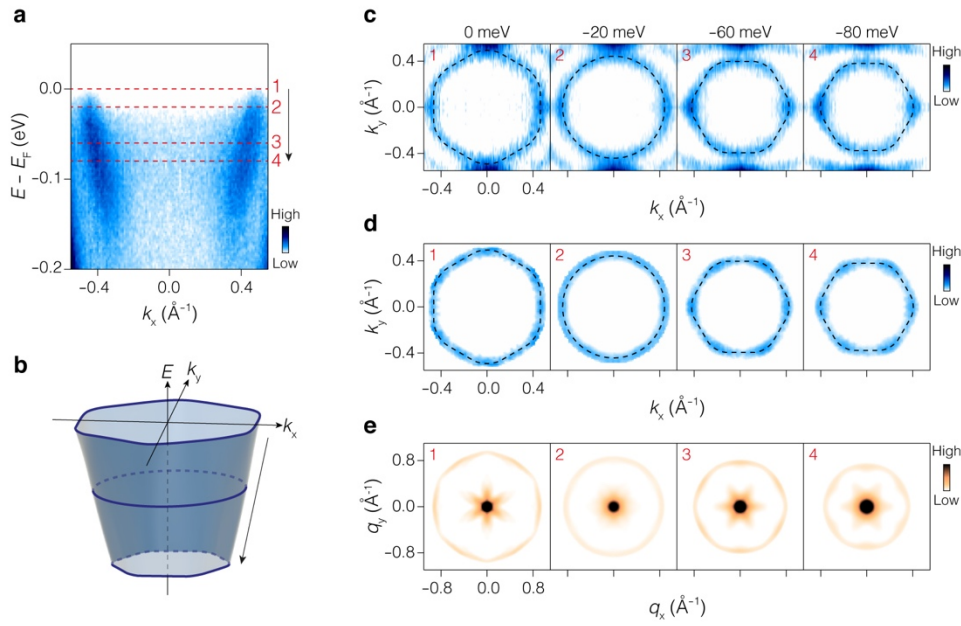
Extended Data Figure 3 | Fermi surface of surface electrons on $[\text{Gd}_2\text{C}]^{2+}\cdot 2e^-$ and photon energy dependence. **a**, In-plane (k_x - k_y) Fermi surface of $[\text{Gd}_2\text{C}]^{2+}\cdot 2e^-$. The black dashed line indicates the BZ. Circular Fermi surface near BZ centre corresponds to the parabolic band dispersion exhibited in Fig. 2a. **b**, Fermi surface in the k_x - k_z plane. The inner straight surface, overlaid by dashed white lines, is from the parabolic band shown in Fig. 2a and from the circular Fermi surface in **a**. **c**, Band dispersion observed at various photon energies from 80 to 108 eV with every 4 eV step to obtain k_x - k_z plane Fermi surface in **b**. **d**, Photon energy-dependent ARPES intensity map extracted from the Fermi level taken with photon energies from 143 to 149 eV, which includes both on- and off-resonant conditions of Gd 4d core level. Dashed grey lines are overlaid on the surface 2D electron band as a guide for the eye. The IAE band intensity at 148 eV greatly increased, a clear resonance behaviour while changing in the intensity of the surface 2D electron band is far weak through the whole photon energies. **e**, Detailed band dispersions at each photon energy in **d** are exhibited.



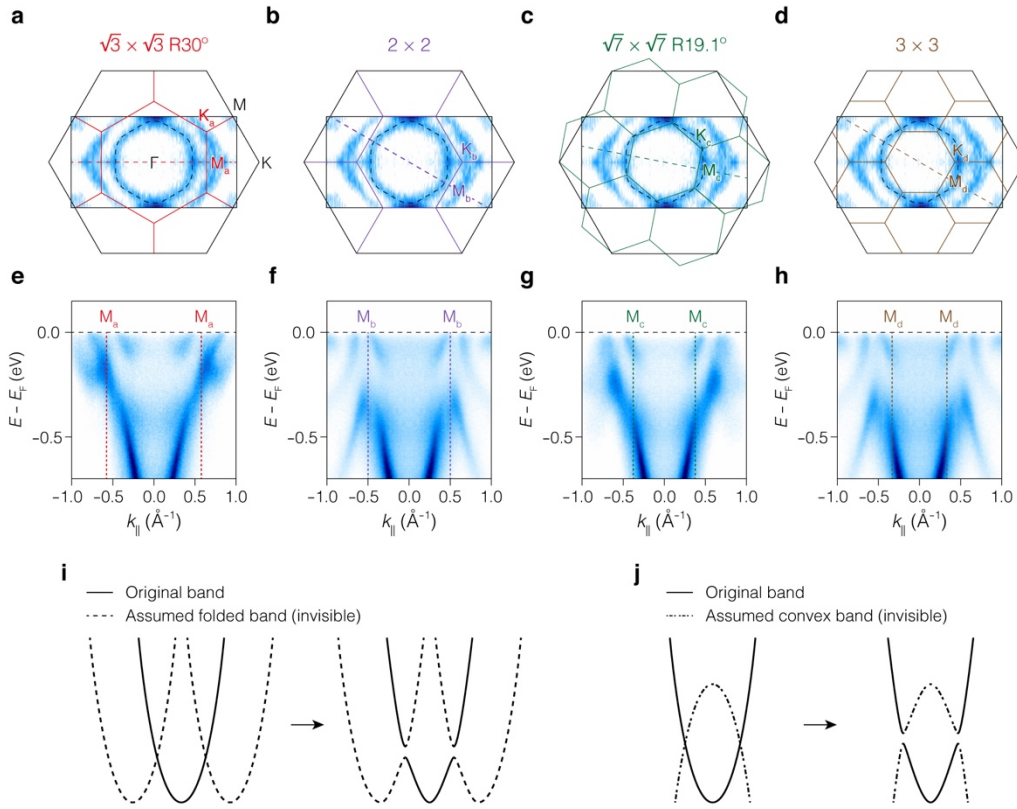
Extended Data Figure 4 | Line shape analysis. a–e, EDCs (blue) taken near Fermi momenta (k_F) along Γ –K direction for different deposition steps #0–#4 in Fig. 4, respectively. To extract the scattering rate shown in Figs. 3c and 4d, EDCs are fitted with a fitting curve generated by multiplication of the Lorentzian curves convoluted with the Gaussian curve for accounting the experimental resolution. Solid black curves represent the result of the fitting. Plotted scattering rates, corresponding to the imaginary part of self-energy, in Figs. 3c and 4d are obtained from the half width at half maximum of the Lorentzian curve for the surface electron band.



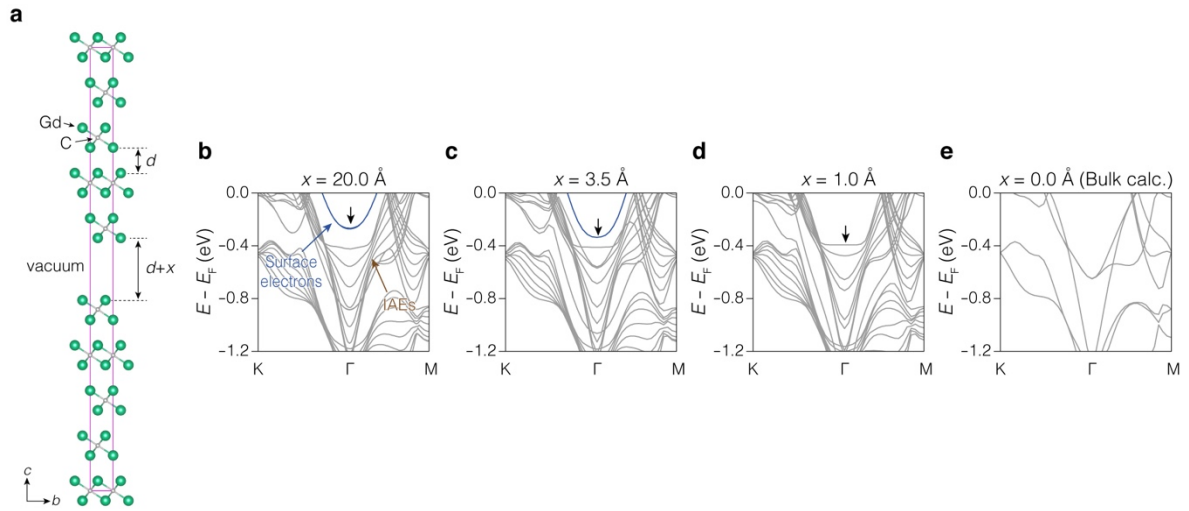
Extended Data Figure 5 | Determination of K coverage. **a**, Core-level spectra of K 3p with different K coverage on the cleaved $[\text{Gd}_2\text{C}]^{2+} \cdot 2\text{e}^-$ surface. The K 3p core-level peak starts to grow with K deposition near the binding energy of 19 eV and eventually saturates where we estimate the coverage as 1 ML (thick green curve). Above 1 ML, chemically shifted additional peaks emerge at lower binding energy close to 18 eV. **b**, A 3D representation of the band evolution with increasing K coverage. **c**, Extracted band dispersion at several different K coverages indicated by red arrows in **b**. Surface 2D electron band (1) evolves via K deposition (2) and disappears (3). This implies the surface electron density is actually reduced by K deposition. In the rightmost panel (4), corresponding to K 1 ML, which we estimate with core-level spectra in **a**, K band appears near Fermi level, which well agrees with the core level estimation.



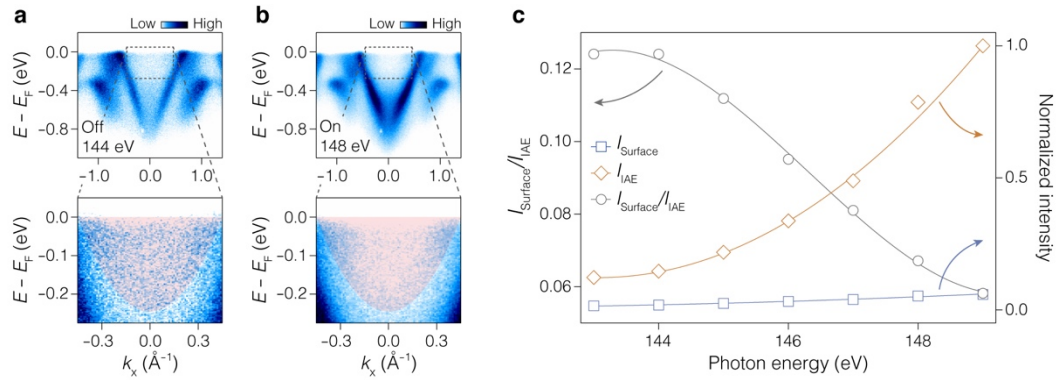
Extended Data Figure 6 | Analysis for the hexagonal topology. **a**, Focused band dispersion of 0.25 ML K coverage, corresponding to deposition step #6 in Fig. 4a. **b**, Schematic band structure of the ARPES result in **a**. Blue solid lines schematically show constant energy contours (CECs) at different energies. **c**, CECs obtained at binding energies of 0, 20, 60, and 80 meV, indicated with dashed red lines (1–4) in **a**. **d**, Symmetrized CECs with 3-fold rotation after removing the intensity from the outer band in **c**, which reveals the shape of energy contours from the quantum electrons more clearly. Overlaid dashed black lines in **c** and **d** are guides for the topology of each CEC. The guidelines evidence that the original shape of contours is not deformed by 3-fold symmetrisation. **e**, Autocorrelation analyses performed with CECs of corresponding energies in **d**, which clearly visualise the angular dependence of the band along with the in-plane momentum.



Extended Data Figure 7 | Scenarios of W-shape band deformation. **a-d**, Fermi surface with 0.25 ML K coverage. BZs of several possible surface superstructures with sub-ML coverage of K, $\sqrt{3} \times \sqrt{3} R30^\circ$ (**a**), 2×2 (**b**), $\sqrt{7} \times \sqrt{7} R19.1^\circ$ (**c**), and 3×3 (**d**), respectively, are overlaid with a different colour. The outermost hexagon with solid black line represents the BZ of 1×1 unit cell of $[\text{Gd}_2\text{C}]^{2+} \cdot 2\text{e}^-$. **e-h**, Observed band dispersion along the Γ - $M_{a,b,c,d}$ direction for new BZs of assumed superstructures at 0.25 ML K coverage. The new zone boundaries by assumed K orderings in **a-d** are overlaid (dashed lines with corresponding colours). Absence of W-shape band at higher momentum above the assumed new zone boundaries, which can be induced by band folding, evidences that W-shaped band deformation is not due to the ordering of deposited K. **i,j**, Schematic drawings of conceivable scenarios for band deformation (hybridisation) by K deposition with assumed zone folded band (**i**) and upward convex band (**j**), respectively. Solid and dashed bands show the original and assumed bands, respectively. Both scenarios may exhibit band deformation, however, they should form the fragment of the original electron band at higher binding energy near BZ centre, which is absent in ARPES results (Fig. 4a).



Extended Data Figure 8 | Band evolution induced by underlying lattice potential. **a**, Crystal structure of the nine-slab model for the slab calculations. The vacuum layer with the thickness x along the c -axis is introduced in addition to the original interlayer space (d). **b–e**, Calculated band structures depending on the vacuum thickness x of 20.0, 3.5, 1.0 and 0.0 Å, where the result of 0.0 Å is obtained by bulk calculation. Black arrows indicate the gradual shift of the surface electron band (blue) downward to the higher binding energy with a decrease in the vacuum thickness x . This exhibits that the surface electron state follows V-shape IAE band when it is strongly affected by underlying lattice.



Extended Data Figure 9 | Resonant ARPES measurement after K deposition. a,b, Band dispersions taken at off- (144 eV, **a**) and on-resonant (148 eV, **b**) condition of Gd 4*d* core level after K deposition (deposition step #6). Lower panels are magnified images of the enclosed area by black dashed box in the upper panels. **c,** Normalised intensity (right) of the surface 2D electrons (I_{Surface} , blue) and trapped IAEs (I_{IAE} , brown), and their ratio (left, gray) as a function of photon energy. I_{Surface} and I_{IAE} are obtained by integrating the intensity of the shaded red area in lower panels and the exclusive area of red shade in upper panels of **a** and **b**, respectively.

Extended Data Table 1 | Comparison of electron liquid on LHe and 2D electride.

	LHe	2D electride ([Gd₂C]²⁺·2e⁻)
Regime	Classical (non-degenerated)	Quantum (degenerated)
Electron density n (cm ⁻²)	~ 10 ⁹	~ 10 ¹⁴
Effective mass m^* (m_e)	~ 1.0	~ 2.1
Fermi energy E_F (meV)	~ 30	~ 250
Temperature T (K)	~ 1	~ 10
Spin polarization	X	O

Figures

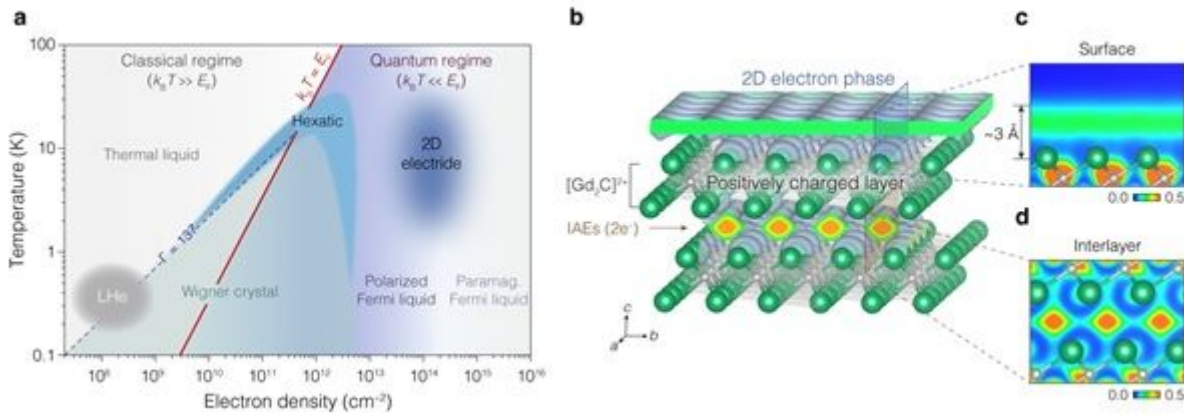


Figure 1

Evolution of pure 2D quantum electrons. a, Phase diagram of pure 2D electron system in terms of electron density and temperature. The solid red line ($k_B T = E_F$) divides the quantum (right) from classical (left) regimes. Colours represent the electron phases; thermal liquid, liquid crystalline hexatic and Wigner crystal in the classical regime, and paramagnetic Fermi liquid, polarised Fermi liquid, hexatic and Wigner crystal in quantum regime. The phase boundaries are estimated from refs. 11, 14-16, 22. The electron phases on the LHe (grey area) are marked from ref. 11. Dashed blue line is the experimental estimation of Coulomb coupling parameter, $\Gamma = 137$ for the Wigner crystallisation in classical regime¹¹. The present pure 2D quantum electrons on the 2D $[\text{Gd}_2\text{C}]^{2+} 2e^-$ electride reside in the area of Fermi liquid (dark blue area). Detailed physical quantities of 2D electrons on LHe and 2D $[\text{Gd}_2\text{C}]^{2+} 2e^-$ electride are compared in Extended Data Table 1. b-d, Visualisation of ELF structures for the electrons on the surface and at the intralayer of 2D $[\text{Gd}_2\text{C}]^{2+} 2e^-$ electride. Cross-sectional plots of the ELF structures for the electrons on the surface (c) and IAEs at the interlayer (d) taken from the blue and brown windows marked in b, respectively.

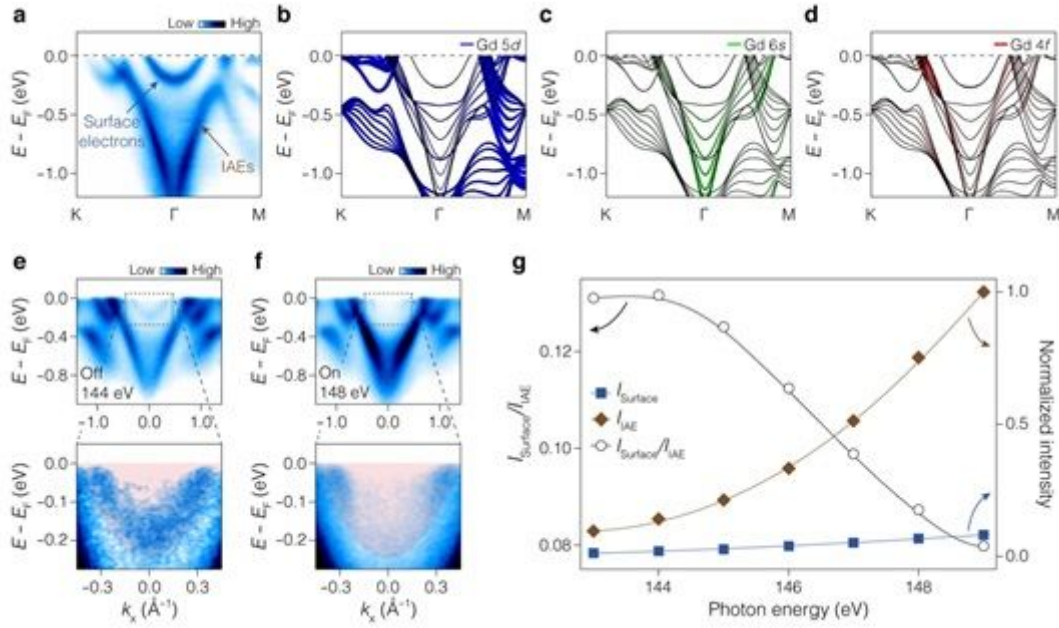


Figure 2

Floating quantum electrons on 2D electride. a, Band dispersion of the 2D [Gd₂C]2+ 2e- observed by ARPES. The blue and brown arrows indicate the parabolic and V-shaped band dispersion from the surface electrons on the terminated [Gd₂C]2+ layer and IAEs trapped between [Gd₂C]2+ layers in the bulk, respectively. b-d, Calculated band dispersions with fat band analysis using the nine-slab model (Extended Data Fig. 2a), exhibiting the contribution of Gd 5d (b), 6s (c), and 4f (d) orbitals. Band thickness with different colours represents the contribution of each orbital; the thicker line has more contribution from the corresponding orbitals. The fat band width in c and d has been magnified by 2 and 3.5 times, respectively, compared with that in b. Almost no colour from each orbital is represented in the parabolic band. e,f, Band dispersions taken at off- (144 eV, e) and on-resonant (148 eV, f) condition of Gd 4d core level. Lower panels are magnified images of the boxed area in the upper panels. g, Normalised intensity (right) of the surface 2D electrons (I_{Surface} , blue) and IAEs (I_{IAE} , brown), and their ratio (left, black) as a function of photon energy (Extended Data Fig. 3d,e). I_{Surface} and I_{IAE} are obtained by integrating the intensity of the shaded red area in lower panels and the exclusive area of red shade in upper panels of e and f, respectively.

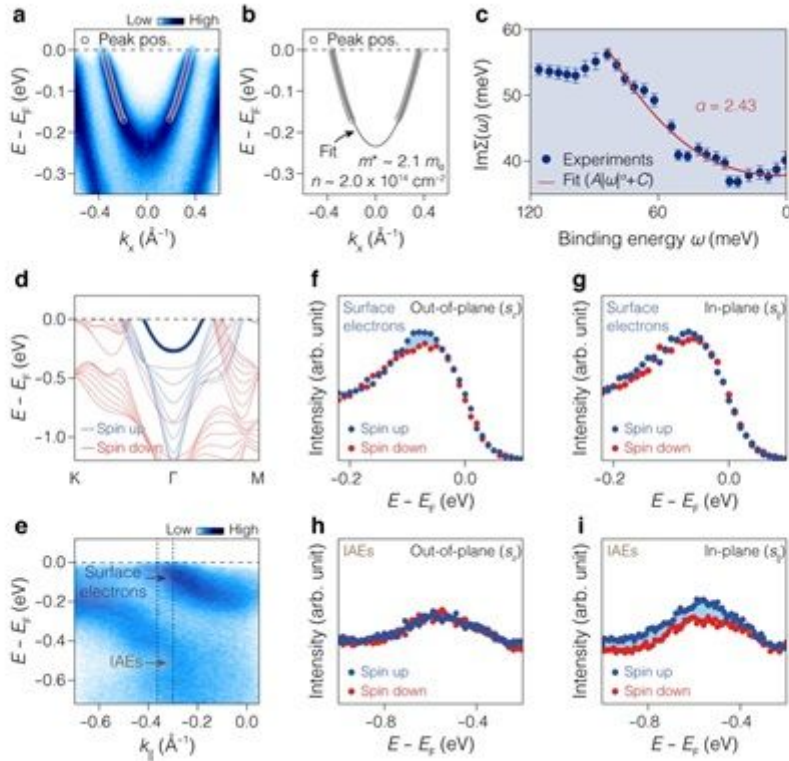


Figure 3

Spin-polarized nature of quantum electron liquid. a,b, Enlarged band dispersion of surface electrons (a). The m^* and n of surface electrons are estimated to be $\sim 2.1 m_e$ and $\sim 2.0 \times 10^{14} \text{ cm}^{-2}$ from the quadratic fitting (black curve in b) of peak positions (white circles) obtained from momentum distribution curves (MDCs) in a. c, Imaginary part of self-energy, $\text{Im}\Sigma$ (filled blue circles), obtained by fitting the energy distribution curve (EDC) width (Extended Data Fig. 4), as a function of binding energy (ω). The solid red curve represents the fit with a power-law ($\text{Im}\Sigma(\omega) = A|\omega|^\alpha + C$). d, Calculated spin-polarised band structure with fat band for the surface electrons. Blue and red colours reflect the spin up and spin down components, respectively. A thick blue band for the surface electrons clearly indicates that the quantum electrons are spin-polarised. For the V-shape bands of the IAEs, spin-polarised state is also shown in the blue colour. e, Measured band dispersion for the spin-resolved ARPES. f-i, Spin-resolved EDCs of surface electrons (f,g) and IAEs (h,i), respectively. Spin up and spin down components are represented by blue and red dots, respectively. EDCs are obtained by integrating intensity within the dashed vertical lines in e.

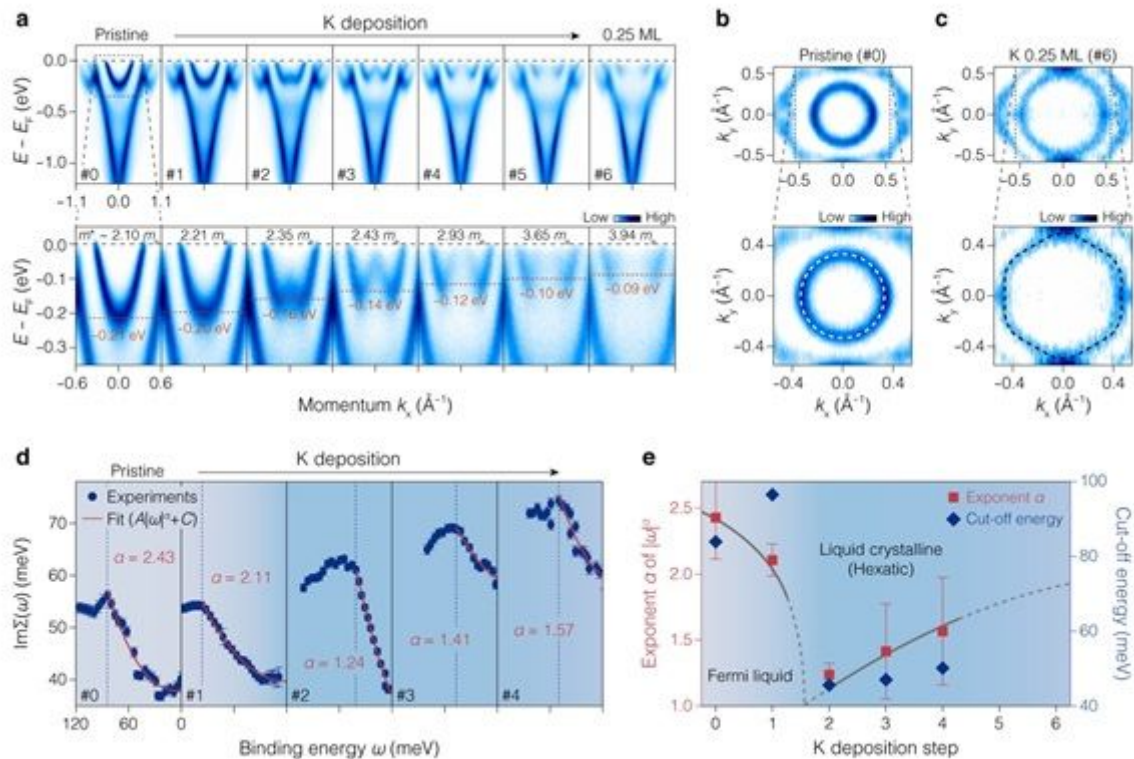


Figure 4

Phase transition of quantum electrons. a, Stepwise evolution of the electronic structure upon K deposition, from the 0 ML (pristine, leftmost) up to 0.25 ML coverage (rightmost). Details of K coverage estimation are described in Extended Data Fig. 5. Lower panels show magnified images (dashed box in the leftmost upper panel) for the band of quantum electrons in each step. Dashed red lines in lower panels represent EBM. b,c, Fermi surface in k_x - k_y plane of the as-cleaved (#0, b) and 0.25 ML K-deposited (#6, c) samples. Lower panels exhibit magnified images of dashed boxes in upper panels. Dashed white circle and dashed black hexagon represent a guide for the eye of Fermi surface topology. d, $\text{Im}\Sigma(\omega)$ for the band of quantum electrons upon K deposition step, extracted by the line shape analysis of EDCs (Extended Data Fig. 4). Solid red curves in each panel are fitted curves of $\text{Im}\Sigma(\omega)$ with a power-law. Dashed blue vertical lines indicate the cut-off energy of $\text{Im}\Sigma$. e, Extracted quantities of exponent α in the $\text{Im}\Sigma(\omega) = A|\omega|^\alpha + C$ and the cut-off energy as a function of the K deposition. Both exponent α (red squares) and the cut-off energy (blue diamonds) show a similar trend, having minima at a specific deposition step (#2) and then increasing toward the initial values upon K coverage. The grey curve is a guide for the eye.

Supplementary Files

This is a list of supplementary files associated with this preprint. Click to download.

- [ExtendedDataFiguresandTables.pdf](#)